A three-dimensional ultrasonic cage for characterization of individual cells

Otto Manneberg,[1] Bruno Vanherberghen,[1] Jessica Svennebring,[1] Hans M. Hertz,[1] Björn Önfelt,[1,2] and Martin Wiklund[1,a]

[1]*Department of Applied Physics, Royal Institute of Technology, KTH-AlbaNova, SE-106 91 Stockholm, Sweden*
[2]*Department of Microbiology, Tumor and Cell Biology, Karolinska Institutet, SE-171 77 Stockholm, Sweden*

We demonstrate enrichment, controlled aggregation, and manipulation of microparticles and cells by an ultrasonic cage integrated in a microfluidic chip compatible with high-resolution optical microscopy. The cage is designed as a dual-frequency resonant filleted square box integrated in the fluid channel. Individual particles may be trapped three dimensionally, and the dimensionality of one-dimensional to three-dimensional aggregates can be controlled. We investigate the dependence of the shape and position of a microparticle aggregate on the actuation voltages and aggregate size, and demonstrate optical monitoring of individually trapped live cells with submicrometer resolution. © *2008 American Institute of Physics.* [DOI: 10.1063/1.2971030]

Microfluidic systems for three-dimensional (3D) contactless manipulation of individual cells or other microparticles are classically based on either dielectrophoresis[1] or optical tweezers.[2] In dielectrophoresis-based systems octopole field cages have long been used for 3D trapping and characterization of single cells,[3] but also for 3D formation and structuring of particle aggregates.[4] Single-beam optical tweezers have been used for 3D trapping and accurate positioning of individual cells.[5] Multiple-beam or holographic optical tweezers have been employed to create 3D structures, lines or arrays of particles.[6,7] Both dielectrophoretic field cages and optical tweezers have been implemented into lab-on-a-chip devices compatible with high-resolution optical microscopy,[1,2,5] and are therefore useful in, e.g., cell characterization applications. However, both techniques require expensive or complicated instrumentation, and suffer from limitations in the long-term (>30min) biocompatibility.[1,8]

In contrast, manipulation devices based on ultrasound have been used for >1h cell retention in microfluidic channels without any loss in viability,[9] and have the potential of being biocompatible for up to several days of operation.[10,11] Even small living animals have been manipulated by ultrasound without evidently changing their state of health.[12] Furthermore, ultrasonic manipulation is a simple, inexpensive, and straightforward method for cell and particle handling. Demonstrated microfluidic-based applications include particle or cell separation, washing, aggregation, and biosensing.[13–15]

In addition to full-channel-actuation systems,[14] semi-closed multiwavelength-size fluidic chambers have been used for multidimensional ultrasonic manipulation of large particle ensembles in microfluidic chips.[16–19] However, no reported ultrasound-based microfluidic device to date is compatible with controlled 3D manipulation of individual microparticles.

In this letter, we demonstrate 3D manipulation of individual microparticles and cells by an ultrasonic cage integrated in a microfluidic chip. The system is compatible with high-resolution optical microscopy allowing on-line observation of intracellular parameters. The ultrasonic cage is designed as a 3D resonant box, which is simultaneously excited at two different frequencies corresponding to half-wave resonances in three orthogonal directions. By tuning the relative actuation voltages at the two frequencies we show 3D particle positioning and enrichment in the center of the cage, and reversible dimensional shape transformation of aggregates containing up to 100 particles. Finally, we demonstrate submicrometer-resolution confocal fluorescence and transmission light microscopy imaging of trapped human immune and kidney cells.

The experimentally observed acoustic properties of the cage are compared with two-dimensional (2D) modeling of the horizontal (top-view) pressure field frequency response in the cage. The pressure field was obtained by numerical simulations using COMSOL MULTIPHYSICS (Ref. 20) with MATLAB (Ref. 21) postprocessing. The acoustic radiation force $\mathbf{F}_{PR}$ is calculated according to[22]

$$\mathbf{F}_{PR} = -\frac{V}{2\rho c^2}\left[\left(1-\frac{\rho c^2}{\rho_p c_p^2}\right)p\,\nabla\,p - \frac{3(\rho_p-\rho)}{k^2(2\rho_p+\rho)}(\nabla p\cdot\nabla)\,\nabla\,p\right], \quad (1)$$

where p is the acoustic pressure, V is the particle volume, k is the wave number, and ρ and c are the density and speed of sound in the medium (no index) and particle (index p), respectively.

Figure 1(a) shows the chip-transducer system. The chip is made of a 14.75×50 mm^2 glass-silicon-glass stack with layer thicknesses of 0.20, 0.11, and 1.0 mm, with the microchannel dry etched in the silicon layer. The cage dimension is $0.30\times0.30\times0.11$ mm^3. The inlet channel cross section is 0.11×0.11 mm^2 [cf. Figs. 1(c) and 1(d)]. The cage was excited by two wedge transducers[22] with nominal resonance frequencies of 2.50 and 6.89 MHz, respectively, which were attached on top of the chip [cf. Fig. 1(a)] by an adhesive gel. All driving voltages were maximum 10 V$_{p.p.}$. The chip design, combined with the transducer placement, allows for high-resolution transillumination microscopy, as well as confocal or epifluorescence microscopy. In the manipulation ex-

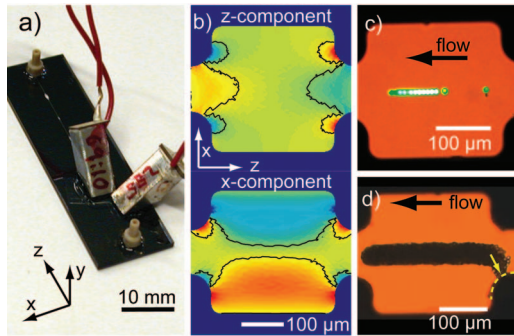[a]Electronic mail: martin@biox.kth.se.

FIG. 1. (Color) (a) Photograph of chip-transducer system. (b) Modeling of the *z* (retention) and *x* (focusing) components of the normalized acoustic radiation force at 2.51 MHz. In the color plot, red is positive, blue is negative, and green is zero. 3D caging of (c) 10 μm beads and (d) 5 μm beads at simultaneous 2.57 and 6.81 MHz actuation (10 $V_{p.p.}$ for both).
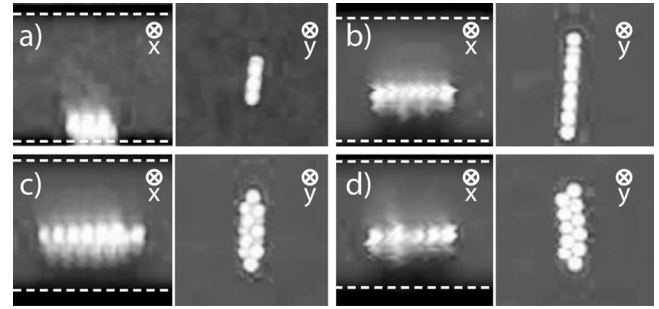

FIG. 2. Demonstration of 3D caging and transformation between a vertical 2D [(a) and (b)], 3D (c), and horizontal 2D (d) bead aggregate positioned with [(b) and (d)] or without (a) a levitation field. For the two actuation frequencies 2.57 and 6.81 MHz, the applied voltages are (a) 7 and 0 $V_{p.p.}$, (b) 7 and 10 $V_{p.p.}$, (c) 4 and 10 $V_{p.p.}$, and (d) 3 and 10 $V_{p.p.}$, respectively. The images are orthogonal 2D cuts extracted from a 3D full-cage confocal microscopy scan. The dotted lines indicate the top and bottom of the channel. The axes refer to the coordinate system in Fig. 1.

periments, we used green-fluorescent 10.4 μm and non-fluorescent 5.0 μm polymer beads, immune cells from a human *B* cell line (721.221) (Ref. 23) labeled with calcein-AM and DiD (Invitrogen), and human embryonic kidney cells (HEK) (293 T).

Figure 1(b) shows simulations of the normalized *x* and *z* components of $\mathbf{F}_{PR}$ [cf., Eq. (1)] for the actuation frequency 2.51 MHz. This frequency is optimized for focusing and retention of particles in the *x* and *z* directions, respectively. The modeling results were compared to flow-through dual-frequency experimental operation at 2.57 and 6.81 MHz. In Fig. 1(c) 10 μm beads are trapped, lined up, and retained close to the center of the cage (slightly displaced downstream due to the viscous fluid drag). Note that the incoming beads enter the cage along the central streamline of the inlet channel due to the additional "funneling" 2D-prealignment function[22] of the levitation field at 6.81 MHz, which is also resonant in the *x* direction in the square-cross-section inlet. The measured trapping efficiency was found to be 100% for enrichment of up to 100 beads at the measured flow speed 1 mm/s (generating $\sim 10^{-11}$ N viscous forces on a trapped 10 μm bead). The loading capacity of the cage was investigated by long-term (overnight) enrichment of 5 μm beads, without considering the trapping efficiency. Figure 1(d) shows the final aggregate containing $\sim 10^4$ beads. Here, we see that such a large aggregate cannot be fully caged in 3D. Beads in the lower right corner are driven to the cage wall, marked with a dotted line in Fig. 1(d). This effect is also predicted in the simulations [cf., corresponding area in Fig. 1(b)]. However, for smaller aggregates (up to a few hundred particles) this effect can be completely avoided by funneling incoming particles by the levitation field [cf., Fig. 1(c)].

The position and shape of a caged aggregate of 10 μm beads was characterized in 3D with confocal microscopy. Figure 2 shows two orthogonal 2D-cut images of an $\sim$10-bead aggregate from a full-cage volume scan. Images are shown for four different combinations of actuation voltages of the levitation (6.81 MHz) and focusing/retention (2.57 MHz) modes. At 7 $V_{p.p.}$ and 2.57 MHz operation only, a 2D aggregate is "standing" vertically (i.e., occupying the *yz* plane) on the bottom of the cage [Fig. 2(a)]. Figures 2(b)–2(d) show dual-frequency operation with different relative actuation voltages, where the aggregate is transformed between standing 2D [Fig. 2(b)], 3D [Fig. 2(c)], and "lying" 2D (i.e., occupying the horizontal *xz* plane) [Fig. 2(d)], re-

spectively. Comparing single-frequency actuation [Fig. 2(a)] with dual-frequency actuation [Figs. 2(b) and 2(d)], we note that the levitation field (6.81 MHz) lifts the aggregate $\sim$40 μm above the channel bottom in Figs. 2(b)–2(d), which corresponds to 3D positioning approximately one cell diameter below the center of the cage. The blurring of the images looking down the *x* axis in Fig. 2 (left panels) is attributable to a combination of the lack of depth resolution, and a slight motion blur caused by the particles moving slightly between consecutive scans of different *xz* planes.

The packaging and structuring of beads during continuous enrichment and aggregation are quantified in the diagram in Fig. 3(a). This is a dynamic study of the experiment shown in Fig. 1(c). The diagram displays the top-view outline and estimated depth of the developing aggregate as a
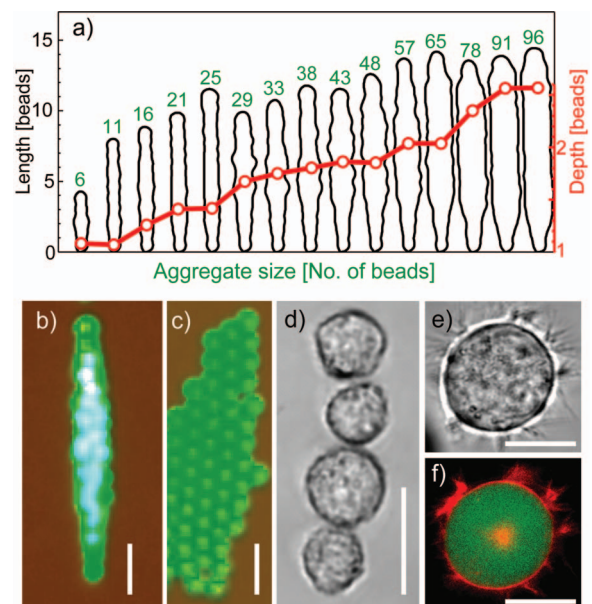

FIG. 3. (Color) (a) Top-view outline (black contours) and average number of layers (red curve) of a developing bead aggregate vs bead number (aggregate size, in green) during flow-through enrichment. Micrograph of a compact 3D (b) and a 2D monolayer (c) aggregate of $\sim$50 beads trapped in the center of the cage. (d) 1D aggregate of four caged HEK cells. [(e) and (f)] High-resolution imaging of a single focused and retained *B* cell labeled with calcein-AM and DiD, dropped to the bottom of the cage. The scale bars are 25 μm in (b)–(d), and 10 μm in (e) and (f).

function of the number of trapped beads, with the aggregate length and depth on the left and right vertical axes, respectively. The outlines are extracted from image analysis of selected frames from a ∼30 s video sequence. Care was taken to select frames of the aggregate in steady state. The aggregate depth is estimated without taking differences in packing density into account. We note that the aggregate undergoes a restructuring into a more compact shape (i.e., shorter and thicker) at certain sizes (e.g., around 25, 38, and 65 beads in [Fig. 3(a)]. These critical sizes depend on the actuation voltages relative to the flow rate. Typically, for <100 bead aggregates the thickness-to-length ratio (i.e., the "compactness") increases as aggregate size and flow rate increase.

When an adequate number of beads or cells have been collected and aggregated it is possible to reversibly transform the aggregate between a compact 3D structure as in Fig. 3(b) and a lying 2D monolayer as in Fig. 3(c). This experiment is performed with ∼50 caged beads at no-flow conditions by decreasing the 2.57 MHz focusing/retention voltage from 10 to 3 $V_{p.p.}$, while keeping the 6.81 MHz levitation voltage constant at 10 $V_{p.p.}$.

Caged cells may be characterized by high-resolution optical microscopy. Figure 3(d) shows four caged HEK cells during medium perfusion. As seen in the image, it is possible to form a one-dimensional (1D) aggregate when the cell number is low enough (approximately <10). More advanced imaging can be performed by dropping the cells to the bottom of the cage (i.e., by turning off the 6.81 MHz levitation field). Figures 3(e) and 3(f) show high-resolution bright-field and confocal fluorescence microscopy imaging, respectively, of a single focused and retained B cell at 2.57 MHz actuation. The micrographs are obtained with a $100 \times / 1.3$ NA oil-immersion objective. The cell is labeled with the green-fluorescent viability indicator calcein-AM, and the red-fluorescent membrane probe DiD. The orange part in the center of the cell indicates an internal membrane, possibly the Golgi apparatus.

To conclude, we have demonstrated 3D caging, enrichment, and shape-specific aggregation, combined with high-resolution imaging of cells or beads in an ultrasonically actuated microfluidic chip. The cage dimension is optimized for individual particle or cell handling, or handling of aggregates containing up to a few hundred particles or cells. Since the cage is simultaneously actuated at two frequencies, it is possible to structure the trapped particles as either a 2D monolayer or a compact 3D aggregate. Monolayer positioning is particularly useful for characterization by (nonconfocal) high-resolution optical microscopy. Transformation between monolayer and multilayer structures is interesting for, e.g., investigation of cell-cell interaction with control of the number of neighbors for each cell.[24] Furthermore, the cage can be used for cell or particle enrichment of very diluted samples due to its 100% trapping efficiency combined with the sample-to-wall preventing funneling (prealignment) function. Future applications include long-term high-resolution monitoring of interactions between individual cells, e.g., the immune synapse,[25] and ultrasensitive bead-based bioanalytics.[13]

[1] T. Müller, A. Pfennig, P. Klein, G. Gradl, M. Jäger, and T. Schnelle, IEEE Eng. Med. Biol. Mag. **22**, 51 (2003).

[2] M. Ozkan, M. Wang, C. Ozkan, R. Flynn, A. Birkbeck, and S. Esener, Biomed. Microdevices **5**, 61 (2003).

[3] T. Schnelle, R. Hagedorn, G. Fuhr, S. Fiedler, and T. Müller, Biochim. Biophys. Acta **1157**, 127 (1993).

[4] S. Fiedler, T. Schnelle, B. Wager, and G. Fuhr, Microsyst. Technol. **2**, 1 (1995).

[5] E. Eriksson, J. Scrimgeour, A. Granéli, K. Ramser, R. Wellander, J. Enger, D. Hanstorp, and M. Goksör, J. Opt. A, Pure Appl. Opt. **9**, S113 (2007).

[6] M. P. MacDonald, L. Paterson, K. Volke-Sepulveda, J. Arlt, W. Sibbett, and K. Dholakia, Science **296**, 1101 (2002).

[7] P. T. Korda, M. B. Taylor, and D. G. Grier, Phys. Rev. Lett. **89**, 128301 (2002).

[8] K. C. Neuman, E. H. Chadd, G. F. Liou, K. Bergman, and S. M. Block, Biophys. J. **77**, 2856 (1999).

[9] J. Hultström, O. Manneberg, K. Dopf, H. M. Hertz, H. Brismar, and M. Wiklund, Ultrasound Med. Biol. **33**, 145 (2007).

[10] I. Z. Shirgaonkar, S. Lanthier, and A. Kamen, Biotechnol. Adv. **22**, 433 (2004).

[11] J. Svennebring, O. Manneberg, and M. Wiklund, J. Micromech. Microeng. **17**, 2469 (2007).

[12] W. J. Xie, C. D. Cao, Y. J. Lü, Z. Y. Hong, and B. Wei, Appl. Phys. Lett. **89**, 214102 (2006).

[13] M. Wiklund and H. M. Hertz, Lab Chip **6**, 1279 (2006).

[14] T. Laurell, F. Petersson, and A. Nilsson, Chem. Soc. Rev. **36**, 492 (2007).

[15] L. A. Kuznetsova and W. T. Coakley, Biosens. Bioelectron. **22**, 1567 (2007).

[16] A. Haake and J. Dual, J. Acoust. Soc. Am. **117**, 2752 (2005).

[17] S. Oberti, A. Nield, and J. Dual, J. Acoust. Soc. Am. **121**, 778 (2007).

[18] S. M. Hagsäter, T. Glasdam Jensen, H. Bruus, and J. P. Kutter, Lab Chip **7**, 1336 (2007).

[19] J. Svennebring, O. Manneberg, P. Skafte-Pedersen, H. Bruus, and M. Wiklund (unpublished).

[20] See http://www.comsol.com/products/multiphysics/

[21] See http://www.mathworks.com/

[22] O. Manneberg, J. Svennebring, H. M. Hertz, and M. Wiklund, "Wedge transducer design for two-dimensional ultrasonic manipulation in a microfluidic chip," J. Micromech. Microeng. (to be published).

[23] Y. Shimizu and R. DeMars, J. Immunol. **142**, 3320 (1989).

[24] P. J. Lee, P. J. Hung, R. Shaw, L. Jan, and L. P. Lee, Appl. Phys. Lett. **86**, 223902 (2005).

[25] D. M. Davis and M. L. Dustin, Trends Immunol. **25**, 323 (2004).